SHORT COMMUNICATIONS

A resonant miniature electric field sensor using bulk-micromachining process*

DENG Kai**, XIA Shanhong, GONG Chao, PENG Chunrong, TAO Hu, BAI Qiang and CHEN Shaofeng

(State Key Laboratory of Transducer Technology, Institute of Electronics, Chinese Academy of Sciences, Beijing 100080, China)

Received October 15, 2004; revised December 22, 2004

Abstract A novel design of a resonant miniature electric field sensor based on microfabrication technology is proposed. The operating principles and specifications, the design structure, and the silicon-based bulk-micromachining fabrication process are presented. The finite element simulation shows that our design can obtain good results in device parameters setting, and its simplicity and low-cost features make it an attractive product for future applications.

Keywords: micro electro mechanical systems (MEMS), bulk-micromachining, anodic bonding, deep reactive ion etching (DRIE).

Recent years, increasing attention has been paid to the research of low-cost and small-sized electric field sensors (EFSs)[1,2] since there exist several applications of their macroscale counterparts[3,4]. For years, a growing development of micromachining technologies has been witnessed, which brought in significant improvement in performance and functionality of various micro electro mechanical systems (MEMS) devices[5,6]. In this paper, we propose a method of designing a miniature EFS (MEFS) using six-step bulk-micromachining process. Advantages of our design in simple fabrication and low cost package are expected to meet the needs of current microsensing market.

The MEFS presented in this paper includes the suspended silicon vibratory frame supported on Pyrex glass wafer with electrodes modulating the spatial electric field periodically. Folded beams and electrostatic excitation are used for vibration driving, which is proved to be efficient in micro inertial measurement unit (MIMU) field[7—9]. The MEFS exhibits advantages in slide-film damping and high quality factor due to its parallel vibrating direction to the membrane surface, which makes the low-cost atmospheric packaging feasible for practical manufacture.

1 Theory

The basic operating principle of MEFS presented in this paper is illustrated in Fig. 1.

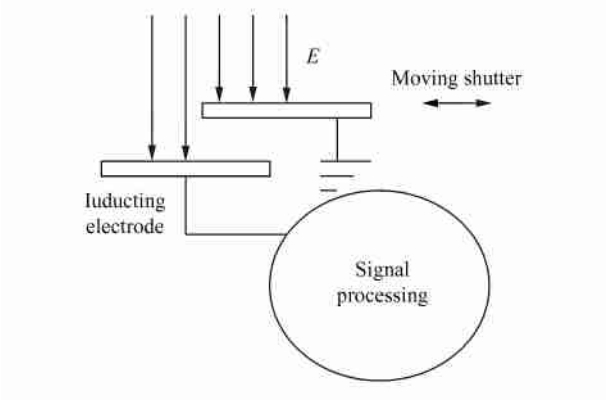

Fig. 1. Schematic diagram of MEFS operating principle.

The upper grounded metal electrode works as a moving shutter to shield the input electric field periodically. The inducting current I can be expressed as:

$$I = \frac{dQ}{dt} = \varepsilon |E| \frac{dA}{dt}, \quad (1)$$

where Q is the inducting charge, A is the effective area of the inducting electrode, E is the spatial electric field, and ε is the dielectric constant of the air. The resulting current is converted into a voltage signal by the amplifier, and it is then amplified and detected to measure the electric field.

* Supported by the National Natural Science Foundation of China (Grant No. 60172001)

** To whom correspondence should be addressed. E-mail: dengkai@tsinghua.org.cn

2 Structure design

Several types of structure are used for electrostatic driving in MIMU field[7, 10, 11]. Figure 2 shows the driving principle of slots structure used in our MEFS. An electric load composed of a dc component V_d and an ac component V_a is applied to the stationary driving electrodes to exert the x-direction driving force on the moving electrodes:

$$F = \frac{2nl\varepsilon V_d V_a}{d}\cos\omega t, \qquad (2)$$

where n is the number of the pairs of driving electrodes, d is the distance between stationary driving electrodes and movable electrodes, l is the overlapping length of the driving electrodes, and ε is the dielectric constant of the air.

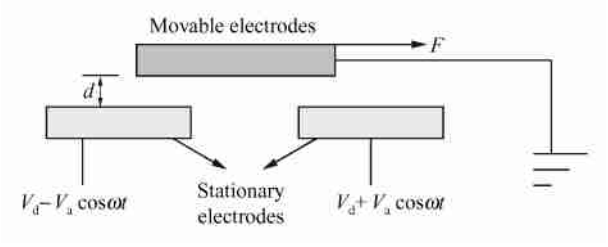

Fig. 2. Driving principle of MEFS.

According to the basic driving principle discussed above, we develop the MEFS structure featuring a suspended silicon vibratory frame anchored to Pyrex glass wafer. The schematic view of the whole device is illustrated in Fig. 3. Several slots are utilized to implement the movable driving electrodes of the silicon structure (Fig. 3 (a)). With metal electrodes sputtered on, the glass bonded to the silicon wafer acts as a supporting substrate and electrodes for electrostatic excitation and measurement of the inducting current (Fig. 3 (b)). Thus, the electric field is modulated by the shielding electrodes in the middle of the silicon wafer and detected by measuring the current from the inducting electrodes on the glass.

The amplitude of the driving force $R(F)$ can be evaluated from Eq. (2). Assuming $n=10$, $V_d = V_a = 16$ V, $d=5\,\mu$m, $l=1760\,\mu$m, we have

$$R(F) = 15.95\,\mu\text{N}. \qquad (3)$$

3 Simulation and analysis

3.1 Dynamical analysis

The mechanical properties of the MEFS were simulated by using ANSYS. For simplification, we

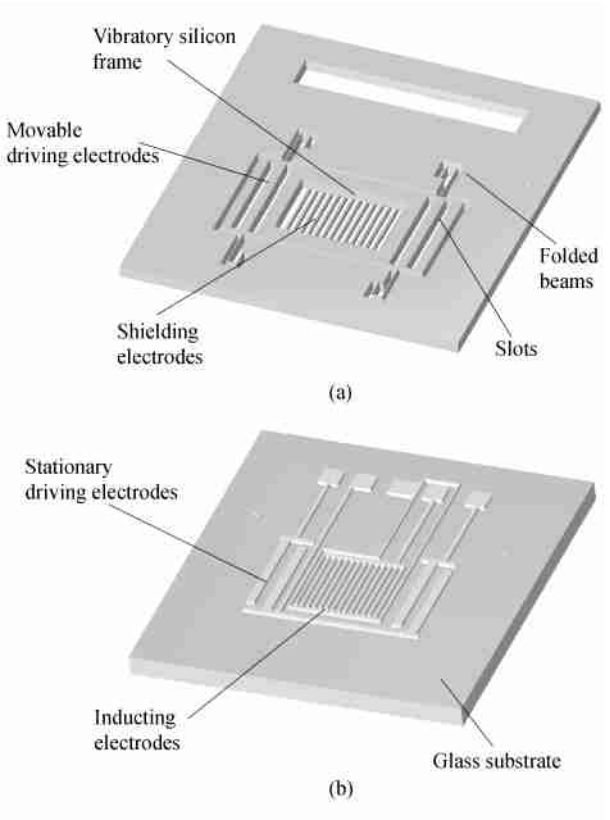

Fig. 3. Schematic view of the (a) MEFS silicon vibrating structure and (b) Pyrex glass substrate with sputtered electrodes.

used a quarter of the MEFS structure as our simulation model (Fig. 4 (a)). The y-direction displacement of the boundary surface ($y=0$) was set at zero, and the x-direction driving force f $\left(f=\frac{1}{4}R(F)=3.988\,\mu\text{N}\right)$ was applied uniformly along the side of each movable electrode. Under such conditions, our simulation results should agree with those of the whole structure.

The simulation results show a maximum x-direction displacement of the silicon structure $S = 0.0586\,\mu$m (Fig. 4 (a)) and a resonant frequency $\nu = 3.867$ kHz (Fig. 4 (b)). Based on the vibration theory, we have the equation of the resonant amplitude R with viscous damping

$$R = \frac{S}{2\xi}, \qquad (4)$$

where ξ is the damping ratio

$$\xi = \frac{c}{2M_0\omega} = \frac{\mu A_i}{2dM_0\omega}$$
$$= \frac{1.648\times10^{-5}\times2\times2.588\times10^{-6}}{2\times5\times10^{-6}\times4.8\times10^{-7}\times2\pi\times3.867\times10^{3}}$$
$$= 7.316\times10^{-4}, \qquad (5)$$

where c is the damping coefficient, μ is the effective

viscosity of the air, A_i is the area of the interface between structure and air, M_0 is the mass of the structure, and ω is the resonant angle frequency of the vibratory frame. So we can obtain the resonant amplitude

$$R = \frac{S}{2\xi} = \frac{0.0586}{2\times 7.316\times 10^{-4}} = 40.04\,\mu\text{m}. \quad (6)$$

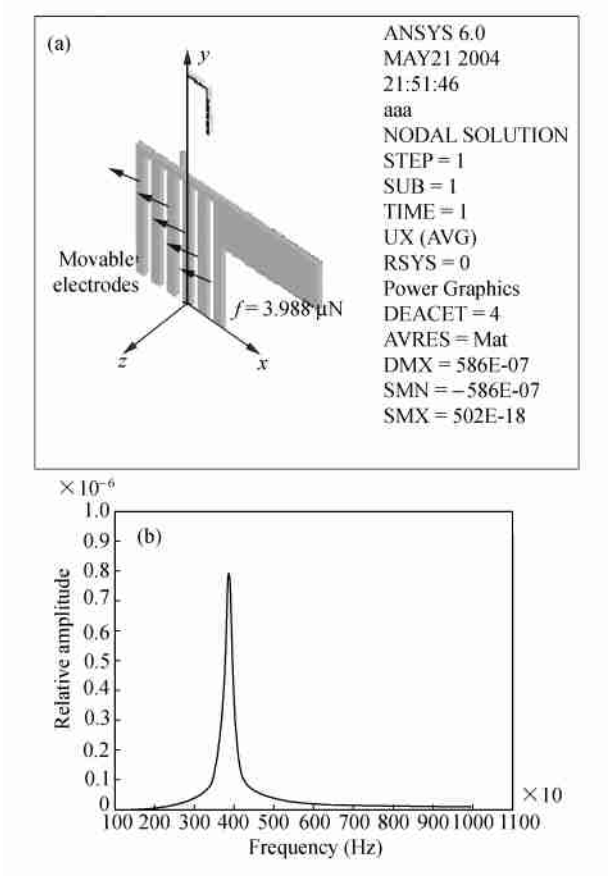

Fig. 4. Simulation results of (a) the mechanical property and (b) the resonant response of a quarter of MEFS by using ANSYS.

3.2 Electrical analysis

According to Eq. (6), we design our shielding and inducting electrodes in the width of 30 μm, which is the efficient size that makes full use of the amplitude while avoiding microfabrication difficulties. The inducting charge following this size is quantitatively described by ANSYS simulation (Fig. 5). The inducting charge q reduces along with the increase in the distance between shielding and inducting electrodes d. The spatial electric field is assumed to be 1000 V/m.

According to the simulation shown in Fig. 5, we set the distance between shielding and inducting electrodes $d = 5\,\mu$m. The corresponding inducting charge

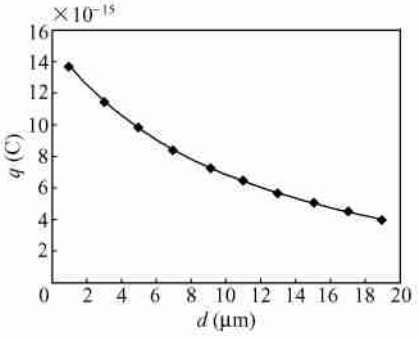

Fig. 5. Inducting charge (q) versus distance between electrodes (d) by ANSYS simulation ($E = 1000$ V/m).

$q = 9.81\times 10^{-16}$ C. With 1000 V/m electric field impinging on MEFS, we can evaluate the inducting current I

$$I = 2qn_0\nu = 2\times 9.81\times 10^{-16}\times 25\times 3.867\times 10^{3} = 1.897\times 10^{-10}\,\text{A}, \quad (7)$$

where n_0 is the number of the shielding electrodes. Table 1 shows the device parameters of our MEFS.

Table 1. Device parameters of MEFS

Parameter of MEFS	Value
Length of driving electrodes: l	2100 μm
Length of shielding and inducting electrodes: l_0	1760 μm
Width of shielding and inducting electrodes: w	30 μm
Distance between shielding and inducting electrodes: d	5 μm
Mass of the silicon structure: M_0	0.48 mg
Beam size: length× width× thickness	(900, 200, 400) μm × 20 μm× 50 μm
Number of driving electrodes: n	10
Number of shielding electrodes: n_0	25

4 Fabrication

Fabrication of the MEFS is based on the silicon bulk-micromachining process (Fig. 6). The starting substrate is a 3-inch n type (100) single-crystalline silicon wafer. A 0.2 μm Si_3N_4 is deposited by low pressure chemical vapour deposition (LPCVD) on silicon substrate as a KOH mask for anchor formation (Fig. 6 (a)). Then a 5 μm-deep silicon etching is performed in KOH solution to form the suspension structure (Fig. 6 (b)). Next, Pt is sputtered on the silicon suspension as the shielding electrodes (Fig. 6 (c)). Then a Pyrex 7740 glass substrate is patterned and Pt is sputtered as stationary driving electrodes and inducting electrodes (Fig. 6 (d)). Next, the silicon wafer and the glass wafer are bonded by anodic bonding (Fig. 6 (e)). Finally, the silicon wafer is

thinned down to 50μm or so by wet chemical etching and DRIE process is utilized to form the slots and beams on silicon wafer (Fig.6 (f)).

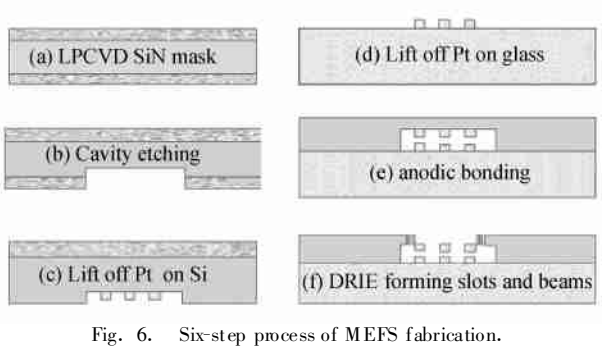

Fig. 6. Six-step process of MEFS fabrication.

5 Summary

An MEFS design based on bulk-micromachining process is described in this paper. Due to the parallel vibrating direction to the substrate surface, the device has advantages in slide-film damping and large vibration amplitude. After discussing its operating principles and analyzing the results, we present the six-step microfabrication process of the device. Advantage of MEFS in simple fabrication and low-cost atmospheric package will widen its potential applications and help its future commercialization.

References

1 Riehl P. S., Scott K. L., Muller R. S. et al. Electrostatic charge and field sensors based on micromechanical resonators. Journal of Microelectromechanical Systems, 2003, 12(5): 577—589.

2 Pei Q., Xia S. H., Gong C. et al. Design and simulation of a miniature electric field sensor based on MEMS technique. Micronanoelectronic Technology (in Chinese), 2003, 40(314/315): 388—390.

3 Kaplan B. Z. and Suissa U. Dynamic models of certain DC and low frequency electric field sensors. IEE Proc. Sci. Meas. Technol., 1997, 144(6): 247—251.

4 Kaplan B. Z. and Suissa U. Duality of the electric covering field-mill and the fluxgate magnetometer. IEEE Transactions on Magnetics, 1998, 34(4): 2306—2315.

5 Sisira K. G., Nihat O. and Henderson H. T. Behavior of bulk micromachined silicon flow sensor in the negative differential resistance regime. J. Micromech. Microeng., 2000, 10: 421—429.

6 Yan G., Zhu Y., Wang C. W. et al. Integrated bulk-micromachined gyroscope using deep trench isolation technology. In: The 17th International IEEE Micro Electro Mechanical Conference. Maastricht, the Netherlands, January 25—29, 2004, 605—608.

7 Xiong B., Che L. F., Wang Y. L. et al. A novel bulk micromachined gyroscope with slots structure working at atmosphere. Sensors and Actuators A, 2003, 107: 137—145.

8 Kuehnel W. and Sherman S. A surface micromachined silicon accelerometer with on-chip detection circuitry. Sensors and Actuators A, 1994, 45: 7—16.

9 Zhu Y. L., Wang S. R. and Qiu A. P. Silicon micromechanical resonant gyroscope. Journal of Chinese Inertial Technology (in Chinese), 2003, 11(4): 45—48.

10 Xiong X. G. and Zou Q. Silicon bulk-micromachined interdigitated differential capacitive accelerometer. Journal of Functional Materials and Devices (in Chinese), 1998, 4(2): 114—120.

11 Fu S. R., Xiong B. and Che L. F. Research on the resolution of fence structure micro-gyroscope under large signal input. Journal of Functional Materials and Devices (in Chinese), 2003, 9(4): 423—427.